



Highly Flexible Superhydrophobic Poly(Urethane Acrylate) Film for Applications Requiring High Optical Transparency

Tian-Feng Hou, Arunkumar Shanmugasundaram, Dong-Su Kim, and Dong-Weon Lee*

The present work elucidates the successful attempts toward the development of a highly transparent, flexible, and superhydrophobic (HTFS) film. The HTFS film is obtained by introducing graphene oxide (GO) into micropillar-patterned poly(urethane acrylate) (PUA), followed by siloxane functionalization via chemical vapor deposition. The fabricated SPG₂ film (siloxane-functionalized PUA incorporated with 0.1 wt% of GO) exhibits a water advancing contact angle, water receding contact angle, and sliding angle of $155.5 \pm 0.3^\circ$, $143.4 \pm 0.6^\circ$, and $9 \pm 0.4^\circ$, respectively. The SPG₂ film also exhibits an optical transmittance of $\approx 84\%$ at 550 nm. Mechanical wearable tests demonstrate no significant degradation in the self-cleaning properties and optical transparency. The fabricated HTFS film (SPG₂) is used as a protective layer for a solar module. This solar module shows improved power conversion efficiency (PCE) compared to that of a bare solar module owing to the high optical transparency and light-trapping effect of the fabricated film that reduce the light reflectance. Furthermore, the SPG₂-protected solar cell demonstrates superior PCE under different surface contamination conditions comparing to other cells. The fabricated micropatterned SPG₂ film can be used for various outdoor applications that require high optical transparency, flexibility, and superior self-cleaning performance.

setae on the feet of geckos.^[3] The importance of superhydrophobic surfaces has been potentially demonstrated in several applications such as anti-fouling,^[4] self-cleaning,^[5] antifriction,^[6] oil/water separation,^[7] microfluidics,^[8] biomedical devices,^[9] and solar cell protection.^[10] However, most proposed superhydrophobic surfaces are nontransparent and inflexible, thereby restricting their use in certain applications such as smart screens for solar panels, camera lens, organic light-emitting diodes, safety goggles, and automobiles.^[11] Therefore, research has focused on realizing a highly transparent, and flexible superhydrophobic (HTFS) surface to overcome these limitations, as well as the drawbacks of the current state-of-the-art flexible transparent films, and thus, expand the range of applications.

A HTFS film requires an optimized surface roughness, a passivation layer comprising functional materials with low surface energy, and a transparent substrate. Recently, several polymer materials like polyethylene terephthalate (PET),^[12,13]

poly(methyl methacrylate) (PMMA),^[14] polydimethylsiloxane (PDMS),^[15] and poly(urethane acrylate) (PUA)^[16,17] have been used to prepare transparent and flexible superhydrophobic films. For example, Teshima et al. fabricated a HTFS substrate via oxygen plasma treatment followed by the deposition of an organosilane hydrophobic coating.^[13] Vourdas et al. prepared a nanotextured superhydrophobic transparent PMMA substrate using a high-density plasma processing method.^[18] However, most PET- and PMMA-based studies conducted oxygen plasma treatment, which is not conducive to large-scale production. On the other hand, PDMS has been widely used to fabricate transparent and flexible superhydrophobic substrates owing to its high fidelity for microstructure development and rapid prototyping. However, it is difficult to prepare a thin PDMS film (tens of micrometers) as a freestanding film or deposit PDMS on other substrates because of its high viscosity and poor adhesion to other substrates.

PUA presents excellent physicochemical and optical properties, such as high deformability, ultraviolet (UV) curability at room temperature, excellent impact strength, and high transparency in the visible region. Despite these beneficial features, to date, experimentally realizing a PUA-based superhydrophobic substrate has seen limited success because of its high surface energy. To the best of our knowledge, only three reports

1. Introduction

Superhydrophobic surfaces have been receiving significant interest in various fields of science and technology owing to their self-cleaning property.^[1] Surfaces with a water contact angle (WCA) greater than 150° and sliding angle (SA) less than 10° are often referred to as superhydrophobic surfaces.^[2] To date, various artificial superhydrophobic surfaces have been fabricated by mimicking natural biological surfaces such as lotus leaves, taro leaves, water strider legs, butterfly wings, and

Dr. T. F. Hou, Dr. A. Shanmugasundaram, D. S. Kim, Prof. D. W. Lee
MEMS and Nanotechnology Laboratory
School of Mechanical Engineering
Chonnam National University
Gwangju 61186, Republic of Korea
E-mail: mems@jnu.ac.kr

Dr. T. F. Hou, Dr. A. Shanmugasundaram, D. S. Kim, Prof. D. W. Lee
Center for Next Generation Sensor Research and Development
Chonnam National University
Gwangju 61186, Republic of Korea

The ORCID identification number(s) for the author(s) of this article can be found under <https://doi.org/10.1002/mame.202000292>.

DOI: 10.1002/mame.202000292

exist on PUA-based HTFS films. Kim et al.^[17] fabricated a nanostructured PUA-based multifunctional self-cleaning transparent surface that presented excellent mechanical robustness. To lower the surface energy and induce strong hydrophobicity, 1H,1H,2H,2H-perfluoro-decyltrichlorosilane was functionalized on PUA via chemical vapor deposition (CVD) at 110 °C for 10 h. Although the material presented excellent optical transparency and hydrophobic nature, the surface modification of PUA with nonecofriendly silane or fluorine poses significant risks to human health and the environment, because long-chain fluoropolymers tend to release substances such as perfluorooctyl carboxylates or perfluorooctyl sulfonates into the environment.^[19,20] Park et al.^[16] fabricated a hydrophobic film using microstructured PUA and a nanosilica spray-coating. The nanosilica-coated PUA film showed high flexibility and transparency with a WCA of $\approx 140^\circ$, but presented poor long-term stability due to insufficient adhesion between the nanosilica and PUA substrate. Huy et al.^[21] developed a highly transparent and flexible siloxane-functionalized micropatterned PUA hydrophobic film. Wet chemical treatment (WCT) of the PUA film with ammonium hydroxide and hydrogen peroxide at 80 °C was necessary to create active functional groups for successful siloxane functionalization. However, the WCT of PUA is a harmful, nonecofriendly, and time-consuming process.

Based on the aforementioned background, considering the advantages of PUA, and to overcome the drawbacks of previous approaches, we herein propose a successful and facile strategy to develop PUA-based HTFS films. Micropillar-patterned PUA was fabricated with different pitch spacings (diameter ($D = 20\ \mu\text{m}$), height ($H = 20\ \mu\text{m}$), and spacing ($S = 20\text{--}100\ \mu\text{m}$)) via a mold transfer process. The inherent hydrophilic nature of PUA was modified into superhydrophobic with siloxane functionalization by CVD at 285 °C using PDMS as a siloxane source. Graphene oxide (GO), which has rich active functional groups and defective chemical sites, was incorporated into PUA to functionalize siloxane on the PUA surface. The siloxane layer on the PUA surface was optimized by incorporating different weight percentages (wt%) of GO, followed by CVD at different temperatures to optimize the WCAs. The HTFS film was characterized by field-emission scanning electron microscopy (FE-SEM), Raman spectroscopy, attenuated total Fourier-transform infrared (ATR-FTIR) spectroscopy, X-ray photoelectron spectroscopy (XPS), and ultraviolet diffuse reflectance spectroscopy (UVDRS) to investigate its morphological, physicochemical, and optoelectronic properties. The SPG₂ film showed excellent hydrophobicity durability during mechanical wearable tests and a high transmittance of $\approx 84\%$ in the visible light region (550 nm). Besides, the fabricated SPG₂ film presented excellent

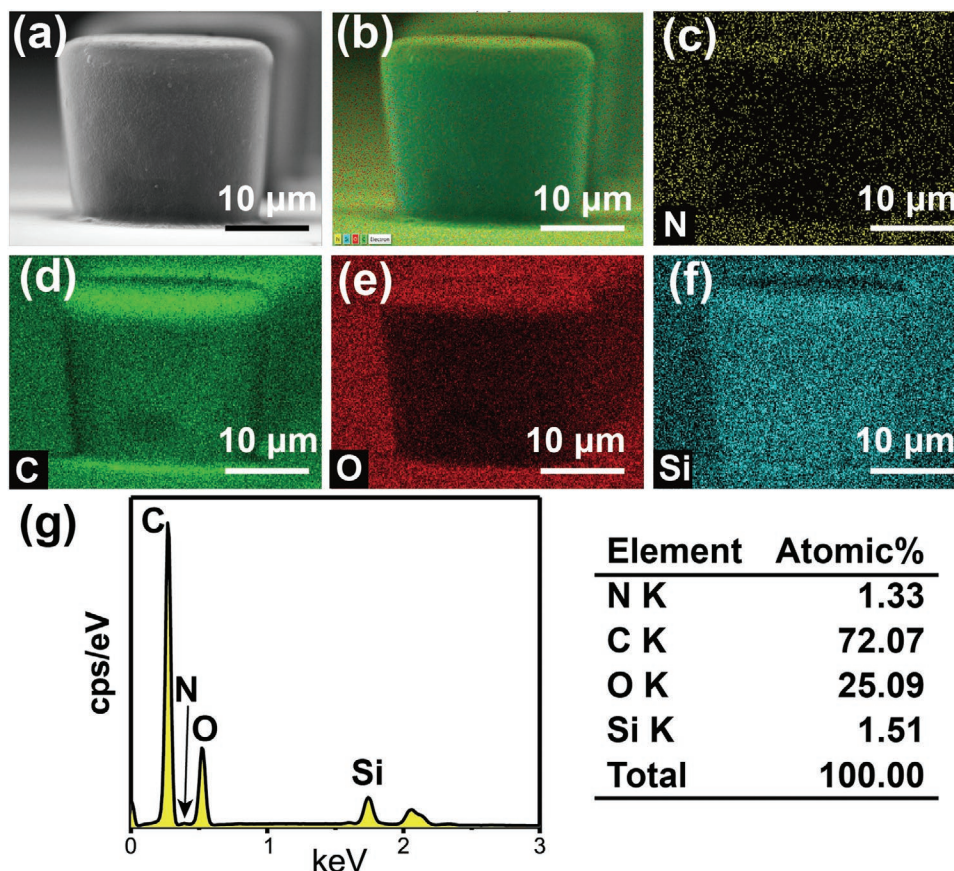


Figure 1. a) FE-SEM image showing the micropillars of the SPG₂ film, b) merged image combining the elemental mapping of the micropillars of the SPG₂ film, c–f) elemental mapping of N, C, O, and Si, and g) corresponding energy-dispersive spectroscopy (EDS) profiles and percentages of the elements on the fabricated SPG₂ film surface.

self-cleaning properties, whether by a gentle wind or by water droplets. Finally, using the proposed film as a protective layer for solar cells, the practical applicability of the prepared SPG₂ film was demonstrated. The SPG₂ film-protected solar module showed significantly improved performance compared to that of a bare solar module due to its high optical transparency and superior self-cleaning ability. Furthermore, the power conversion efficiency (PCE) of the solar cells protected by the sand-contaminated SPG₂ film could be recovered to the original value after eliminating the sand contamination via subsequent cleaning by wind and water droplets.

2. Results and Discussion

2.1. Characterization of Siloxane-Functionalized Film

FE-SEM was performed to study the morphology of the fabricated PG₂ film before and after siloxane functionalization, as shown in Figure S1 (Supporting Information). The diameter, height, and spacing of the micropillar were found to be ≈ 20 , ≈ 20 , and ≈ 50 μm , respectively (Figure S1a,b, Supporting Information). After siloxane functionalization, a very thick layer was observed on the SPG₂ film, confirming the successful deposition of siloxane on the PG₂ surface by PDMS CVD (Figure S1c,d, Supporting Information). The unreacted siloxane group was removed from the SPG₂ film by ultrasonication with ethanol for 30 min; the corresponding FE-SEM image is shown in Figure 1a. The SPG₂ film retained the parent morphology of PG₂, indicating the nondestructive nature of PDMS CVD.

Figure 1b–f shows the elemental mapping of the fabricated SPG₂ film. The uniform distributions of nitrogen (N), carbon (C), oxygen (O), and silicon (Si) indicate that a siloxane monolayer is deposited on the PG₂ film surface. Figure 1g shows the energy-dispersive spectrum and the corresponding element atomic percentage of the fabricated SPG₂ film. The atomic percentages of N, C, O, and Si were found to be ≈ 1.33 , 72.07, 25.09, and 1.51, respectively.

The FTIR and Raman spectra were analyzed to study the surface chemistry of the as-fabricated SPG₂ film and the mechanism of siloxane functionalization of the SPG₂ surface by PDMS CVD. Figure 2 shows the ATR-FTIR spectra of the as-prepared GO, PUA, PG₂, and SPG₂ films. The ATR-FTIR spectrum of GO (Figure 2i) exhibits an intense band at 3445 cm^{-1} and a broad band at 3300–2925 cm^{-1} , which were assigned to the stretching vibrations of hydroxyl (O–H) at the edge of GO and carboxylic acid groups (–COOH), respectively.^[22] The band at 1723 cm^{-1} was associated with the stretching of C=O in carboxylic acid groups (–COOH).^[23] The peak at 1583 cm^{-1} corresponded to C=C–C stretching in the aromatic ring. The peaks at 1400 cm^{-1} and 1206 cm^{-1} were assigned to O–H bending and C–O stretching in the phenol groups, respectively. The peaks at 1124 and 836 cm^{-1} were attributed to C–O– stretching in the epoxy ring.^[24]

The ATR-FTIR spectra of PUA and PG are shown in Figure 2ii,iii. In the spectrum of PG, except for the absorption band at 3680 cm^{-1} which was associated with –OH, several new absorption bands assigned to PUA were observed. Peaks at 723, 793, 843, and 872 cm^{-1} were associated with aromatic C–H out-of-plane bending. Peaks at 968 and 1016 cm^{-1} were assigned to

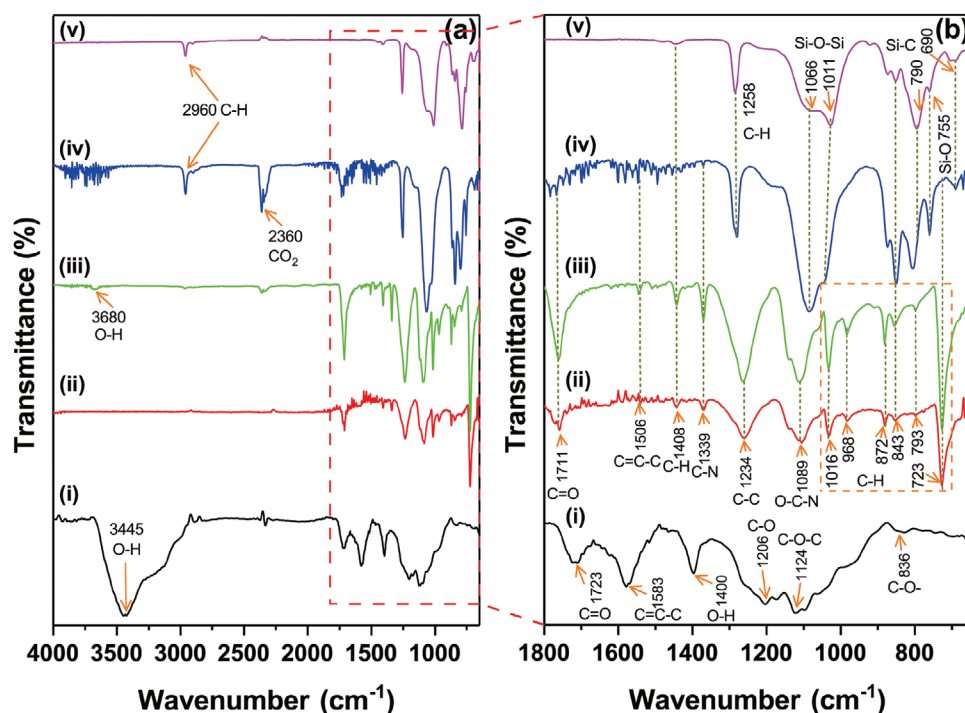


Figure 2. ATR-FTIR spectra of the i) GO, ii) PUA, iii) PG₂, iv) SPG₂, and v) PDMS elastomer. a) Wavenumber range from 4000 to 650 cm^{-1} and b) enlarged view from 1800 to 650 cm^{-1} .

C–H in-plane bending. Other peaks at 1089, 1234, 1339, 1408, 1506, and 1711 cm^{-1} were assigned to OCN stretching, skeletal C–C vibrations, C–N stretching, C–H in-plane bending, aromatic ring stretching (C–C–C), and C=O stretching in a carboxylic acid group (–COOH). With the siloxane functionalization layer, some new peaks associated with the siloxane groups appeared in SPG₂ (Figure 2iv), and were consistent with those in the spectra of the PDMS elastomer (Figure 2v). The peaks at 2960 and 1258 cm^{-1} were assigned to the C–H antisymmetric and C–H symmetric stretching of Si(CH₃)₂ groups from the siloxane.^[25] The wide band at 1000–1100 cm^{-1} was associated with the stretching vibration of Si–O–Si. The bands at 1011 and 1066 cm^{-1} were attributed to the stretching vibration of Si–O–Si in the cyclic-D₃/D₄ and linear siloxanes, respectively.^[26] The peaks at 790 and 690 cm^{-1} were assigned to Si–C stretching.^[27] The peak at 755 cm^{-1} was associated with the perpendicular vibration of Si–O.^[28] The band at 2360 cm^{-1} was due to atmospheric CO₂.^[29]

To characterize the properties of GO, Raman spectroscopy was performed. The Raman spectra of GO and the prepared films of PUA, PG₂, and SPG₂ are shown in Figure 3. The Raman spectrum of GO (Figure 3i) showed a D band at 1357 cm^{-1} , which is comparable in intensity to the G band at 1594 cm^{-1} . The D and G bands arise due to the out-of-plane breathing mode of the sp² atom and E_{2g} phonons of carbon, respectively.^[30] The D-to-G-band intensity ratio (I_D/I_G) was ≈ 1.04 , which indicates that GO has a distinct structural disorder due to the harsh oxidation conditions in Hummers' method. The bands observed at 2709 and 2932 cm^{-1} correspond to 2D and D+G, respectively. The spectrum of PUA (Figure 3ii) displays characteristic bands at 1619, 1730, 2930, and 3085 cm^{-1} , which were assigned to the aromatic ring (C–C) model, stretching vibration of the C=O band, methylene groups adjacent to oxygen atoms, and aromatic C–H bonds, respectively.^[31] The spectrum of PG₂ (Figure 3iii) shows the characteristic bands of both, PUA and GO. The D and G bands were shifted to higher wavenumbers and were broadened due to the interaction between PUA and GO. The Raman spectrum of SPG₂ (Figure 3iv) showed a band at 2937 cm^{-1} , assigned to the –CH₃ antisymmetric stretching vibration of siloxane,^[32] which was confirmed by the Raman spectrum of the PDMS elastomer (Figure 3v). In the spectrum, the bands at 491 and 623 cm^{-1} were assigned to Si–O–Si stretching, the band at 709 cm^{-1} was associated with Si–C symmetry stretching, the band at 1407 cm^{-1} was attributed to the asymmetric bending of C–H in –CH₃, and the bands at 2944 and 3004 cm^{-1} were due to the asymmetric stretching of C–H in –CH₃.^[33]

To further derive important chemical and structural information on the surface of SPG₂, XPS was performed. Owing to the charging effects caused by the insulating property of the samples, a C 1s binding energy of 285 eV was used for peak correction of the samples. Peaks assigned to carbon (C 1s at 284.60 eV), oxygen (O 1s at 531.98 eV), nitrogen (N 1s at 398.59 eV), and silicon (Si 2p at 101.14 eV) were present in the survey spectra (Figure S2, Supporting Information). Table S1 (Supporting Information) provides the binding energy and atomic concentrations of the different elements in SPG₂.

Figure 4a shows the deconvoluted C1s spectrum of the SPG₂ film. The peak at 288.01 eV could be indexed to the C=O from

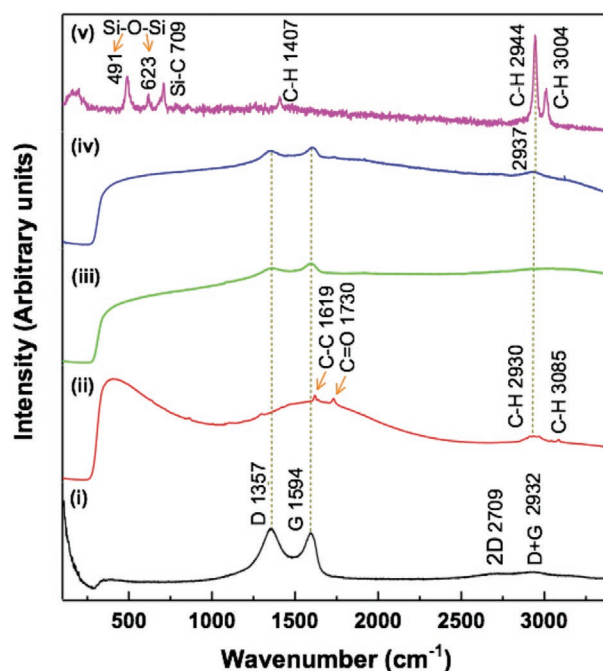


Figure 3. Raman spectra of GO, PUA, PG₂, SPG₂, and the PDMS elastomer.

the carboxyl and carbonyl groups.^[34] The peak at 285.9 eV was attributed to the C–O of esters, epoxy, alkoxy, or carboxyl;^[35] C–OH; and C–N, respectively.^[34,36] The peak at 284.6 eV was associated with C–C sp²-hybridized carbon.^[37–39] The peak at 283.2 eV was assigned to the formation of the C–Si bond.^[40] Figure 4b shows the deconvoluted O1s spectrum of the SPG₂ film. The peak at ≈ 533.4 eV was attributed to the C–O bond of O–C(=O)–N and O–H of –COOH.^[41] The peak at 532.01 eV corresponded to the C=O and Si–O of ((Si(CH₃)₂–O–)_n) bonds.^[42] The peak at 530.46 eV corresponded to the quinones of GO.^[43] Figure 4c shows the N1s core-level spectrum of the SPG₂ film. The peak at 399.16 eV was attributed to N–C and N–H.^[34,44] Figure 4d shows the Si2p core-level spectrum of the SPG₂ film. The peak observed at 101.18 eV was attributed to the Si–O–Si bond resulting from siloxane functionalization on the surface of PG₂.

2.2. Plausible Mechanism for the Formation of SPG Hybrid Superhydrophobic Structure

Siloxane functionalization on an inorganic oxide surface through PDMS CVD has been reported previously.^[26,45] The –OH groups on the substrate surface were found to be vital in siloxane functionalization. In this work, we successfully functionalized siloxane on the PG surface. First, GO was prepared by the modified Hummers' method (Scheme 1a,b). Subsequently, the GO was mixed with the prepolymer of aromatic urethane multifunctional acrylate and a photoinitiator under ultrasonication (Scheme 1c). The GO sheets were uniformly distributed in the mixture. During UV curing, polymerization was initiated by the photoinitiator, which fragmented into free radicals when mixing the resin under UV exposure. The free radicals reacted

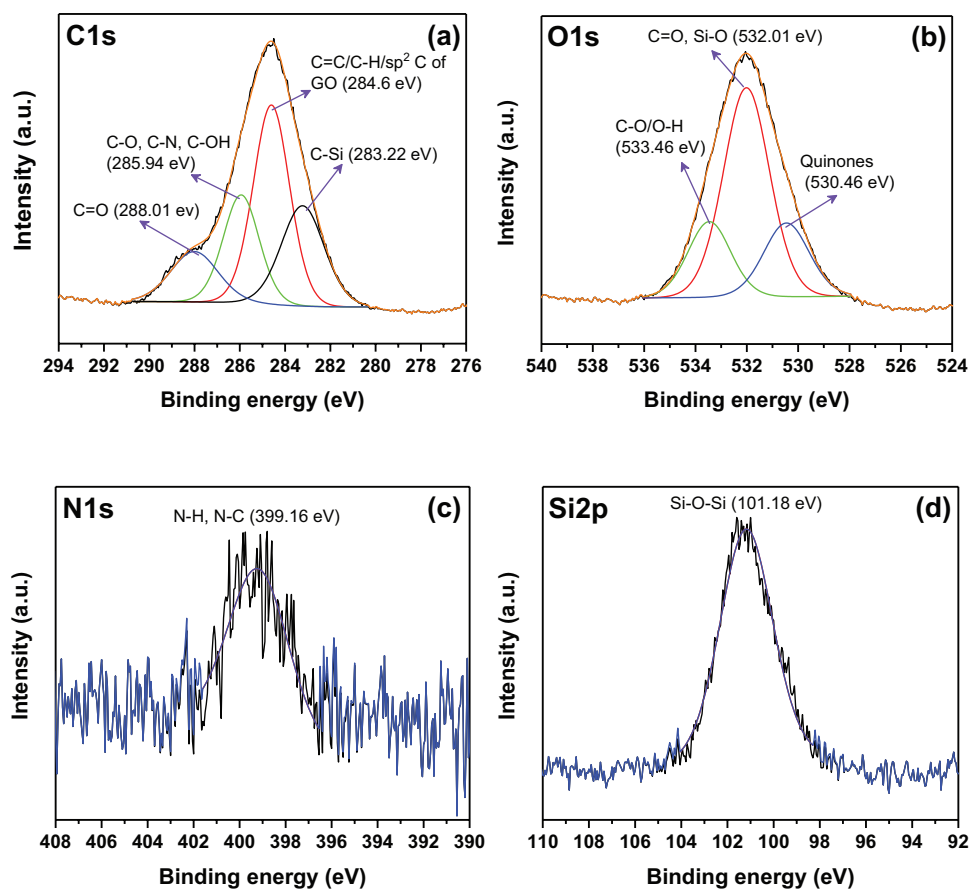


Figure 4. XPS profiles of the fabricated SPG₂ film. Core-level spectra of a) C1s, b) O1s, c) N1s, and d) Si2p.

with the aromatic urethane acrylate by attaching to the caps of acrylate (Scheme 1d). Several active functional groups such as hydroxyl, carboxyl, carboxylic, and epoxide were introduced by the incorporation of GO into PUA.

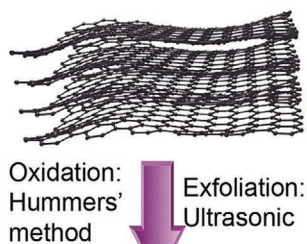
Water was significantly absorbed on the high-energy surface even at a relative humidity as low as 0.6%.^[46] However, Jiao et al. reported that the water on the surface acts as a barrier layer and plays a key role in preventing the surface from reacting with the siloxane molecules.^[26] Therefore, the bonded water molecule needs to be removed from the substrate by a thermal or any other technique. During PDMS CVD, the PDMS prepolymer was heated to its boiling point (≈ 220 °C), while the temperature of the PG substrate was detected to be ≈ 150 – 175 °C. The long chains of PDMS were gradually dissociated into small molecular segments, including linear and cyclic chains (D3 and D4) of siloxane oligomer fragments/oligomers (Scheme 1e).^[47] Subsequently, the chemical reaction between these siloxane oligomer fragments/oligomers and the heat-treated PG surface commenced. Vapor-phase siloxane was assumed to covalently attach to the PG surface through the reactions between the surface hydroxyl groups and vapor-phase siloxane groups (Scheme 1f). The vapor-phase linear or cyclic siloxane fragments/oligomers can react with the hydroxyl group on GO through the following steps: I) direct covalent bonding between hydroxyl groups and vapor-phase siloxane groups; II) with

increasing deposition time, the bonded siloxane fragments/oligomers can be crosslinked with each other; and III) covalent attachment by the addition of siloxane fragments/oligomers, resulting in complete coverage and a slight increase in the thickness of the covalently bonded siloxane-functionalized layer. Thus, the hydroxyl groups introduced by GO play a key role by reacting with the siloxane groups that were evaporated by heating the PDMS prepolymer.

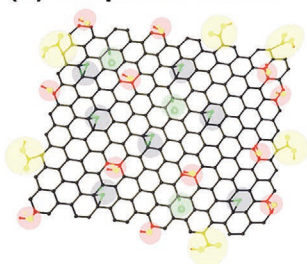
2.3. Wettability, Flexibility, Transparency, and Self-Cleaning Properties

Films with different micropillar spacings were fabricated to optimize the superhydrophobic properties of the siloxane-functionalized films. All fabricated films had micropillars with a diameter and height of ≈ 20 μm . The space between the micropillars was varied from 20 to 100 μm . Figure S3 in the Supporting Information shows the FE-SEM images of the fabricated micropatterned SPG₂ films. The hydrophobicity of the SPG₂ films was evaluated by measuring the WCA, water advancing contact angle (WACA), water receding contact angle (WRCA), and SA with different micropillar spacings. The WCA of the SPG₂ film with a space of 20 μm was found to be $\approx 134.5^\circ$ (Figure 5a). The WCAs of the SPG₂ films increased

(a) Graphite oxide

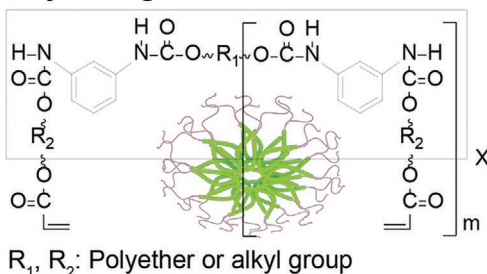


(b) Graphene oxide



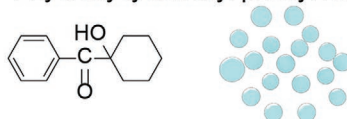
(c) UV-curable PUA resin

(i) Aromatic urethane multifunctional acrylate oligomer



(ii) Photoinitiator

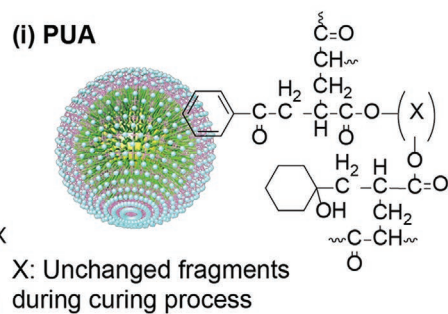
1-hydroxycyclohexyl phenyl ketone



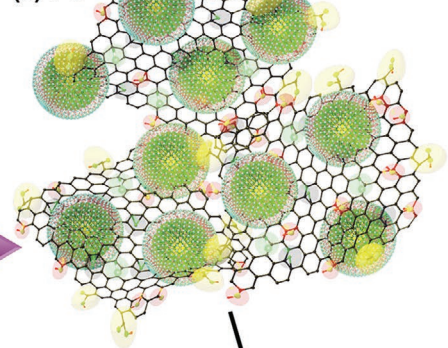
Mixing: Ultrasonication
Curing: photopolymerization

(d) Micropillar patterned film

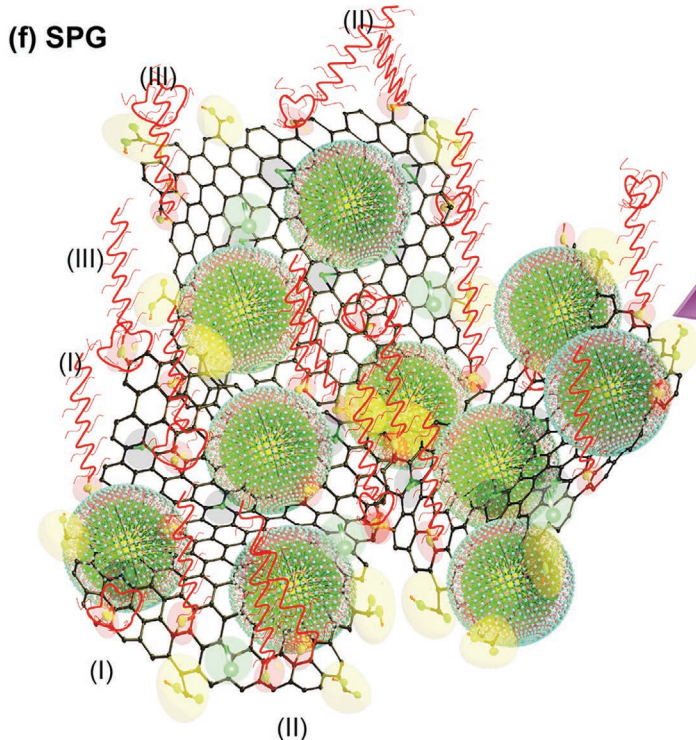
(i) PUA



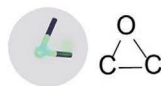
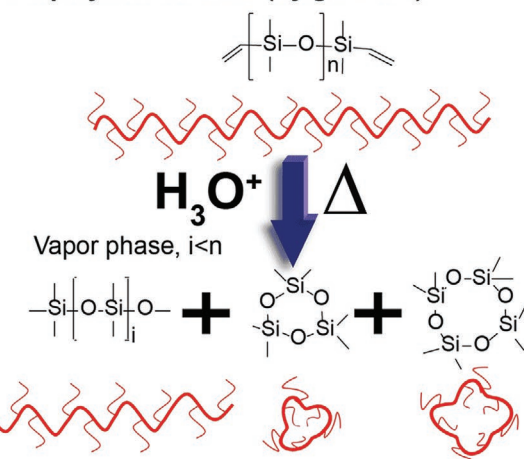
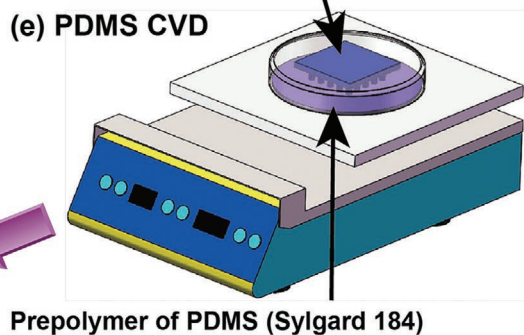
(ii) PG



(f) SPG



(e) PDMS CVD



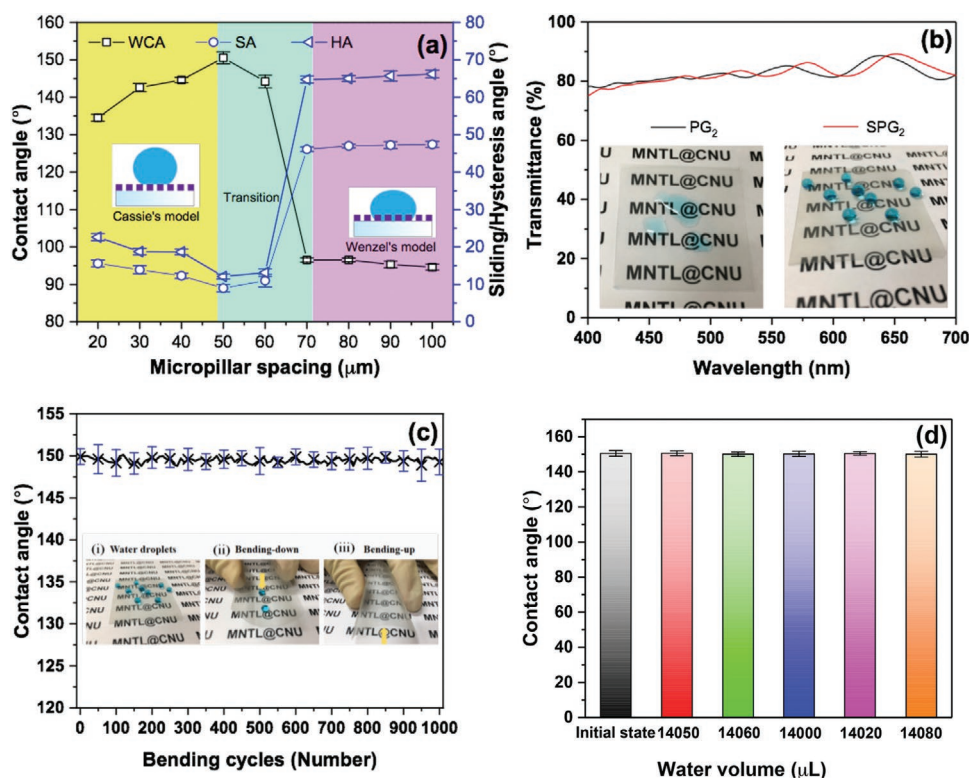


Figure 5. Superhydrophobicity, transparency, flexibility, and robustness of the fabricated SPG₂ film under water-droplet impact a) WCAs, SA, and HA of the SPG₂ film with varying micropillar spacing ranging from 20 to 100 μm. b) UV-vis transmittance spectra of the PG₂ and SPG₂ films (50 μm spacing). The insets in panel (b) show the photographs of water droplets deposited on PG₂, and SPG₂, respectively. c) WCAs of SPG₂ (50 μm spacing) as a function of bending cycles. The insets in panel (c) show the optical images of the SPG₂ film with water droplets deposited on the surface, downward-bending, and upward-bending positions. d) WCAs of the SPG₂ film after repeated water-droplet impact.

with increasing spacing between the micropillars and reached the maximum value of 150.5° at a pillar spacing of 50 μm. The WCAs of the SPG₂ films decreased with a further increase in the micropillar spacing. The WCAs slightly decreased from 150.5° to 144.2° at the pillar spacing of 60 μm, and substantially decreased to 96.5° at the pillar spacing of 70 μm. These results indicate that the wetting state begins to transit from the Cassie–Baxter state to the Wenzel state at a micropillar spacing of 50 μm, and completes the transition at micropillar spacings greater than 60 μm. The transition of the wetting state can be realized by changing the geometric parameters of the underlying surface, as reported by Jung and Bhushan.^[48] The apparent contact angles for the water droplets under the Wenzel state (θ_r^w) and Cassie–Baxter state (θ_r^c) can be expressed as^[48,49]

$$\cos \theta_r^w = \left(1 + \frac{\pi DH}{(S+D)^2} \right) \cos \theta_0 = \left(1 + \frac{\pi B}{(D/H)} \right) \cos \theta_0 \quad (1)$$

$$\cos \theta_r^c = \frac{\pi D^2}{4(S+D)^2} (\cos \theta_0 + 1) - 1 = \frac{\pi}{4} B (\cos \theta_0 + 1) - 1 \quad (2)$$

where

$$B = \frac{1}{\left(\frac{S}{D} + 1 \right)^2} \quad (3)$$

Here, D , S , and H are the diameter, spacing, and height of the micropillars, and θ_0 is the WCA on the flat surface ($\approx 97.6^\circ$ in the present work). According to the equations, θ_r^c is independent of D/H , whereas θ_r^w is dependent on both S/D and D/H . The transition of the wetting state can be realized by changing the geometric parameters of the underlying surface. In the present work, the wetting state of the fabricated SPG₂ film was found for a S/D less than 2.5 (Figure 5a). Therefore, changes in the diameter and height of the micropillar will not affect the wetting properties of the film with a S/D less than

Scheme 1. Schematic illustration of the preparation of the PG composite and a proposed mechanism for the subsequent siloxane functionalization of the surface by PDMS CVD. a, b) Synthesis of GO by Hummers' method followed by ultrasonication exfoliation, c) mixing of GO with the prepolymer of aromatic urethane multifunctional acrylate and a photoinitiator under ultrasonication, d) cured PUA and PG, e) thermal decomposition of the prepolymer of PDMS, and f) siloxane functionalization of the PG surface by PDMS CVD.

2.5. Figure S4 (Supporting Information) shows the measured WCAs and the qualitative plot of the apparent contact angles for the Wenzel and Cassie–Baxter states with respect to the normalized spacing ratio by the pillar diameter (S/D). The measured WCAs were consistent with the changing trend predicted by the Cassie–Baxter equation when S/D was less than 2.5, whereas they rapidly decreased and were consistent with the changing trend predicted by the Wenzel equation for a higher S/D .

Figure S5 (Supporting Information) shows the WACAs and WRCAs of the SPG₂ films with different micropillar spacing. The WACAs of the SPG₂ films increased with increasing micropillar spacing from 20 to 50 μm and then saturated. The WRCAs of the SPG₂ films first increased with the micropillar spacing and reached a maximum value of 143.4° at the micropillar spacing of 50 μm . Subsequently, the WRCAs slightly decreased to 141.9° at 60 μm , followed by a sharp decrease to 91.0° at 70 μm . Finally, the WRCAs of the SPG₂ films slightly decreased with a further increase in the micropillar spacing to 100 μm .

The SA and hysteresis angle (HA) of the SPG₂ film with varying micropillar spacing are shown in Figure 5a. The HA was calculated from the WACA and WRCA of the SPG₂ film. The SA and HA plots showed opposite trends compared to the WCA with varying pillar spacing. The SA and HA of the SPG₂ film at 20 μm were 15.6° and 22.6°, respectively; they decreased with increasing pillar spacing up to 50 μm ($\approx 9^\circ$, and 12.1°, respectively), and subsequently sharply increased to 46.1° and 64.7° with a further increase in the micropillar spacing. The SA and HA of the SPG₂ film verify the change in the wetting state, which can be explained as follows. When the micropillar spacing was increased from 20 to 50 μm , a composited interface (air pocket) was successfully formed, resulting in a stable and superhydrophobic surface. However, it was difficult to maintain the composite interface with a further increase in the micropillar spacing. Consequently, the air pockets were lost, and completely eliminated for the SPG₂ surface with micropillar spacings of 60–100 μm . In conclusion, the SPG₂ film with a micropillar spacing of 50 μm showed superior hydrophobicity.

Figure 5b shows the UV–vis spectra of the PG₂ and SPG₂ (50 μm spacing) films with the percent transmittance at 400–700 nm. Both films showed more than $\approx 84\%$ transmittance in the visible light range. The inset in Figure 5b shows the photograph of the fabricated PG₂ and SPG₂ films. The high transparency of the fabricated film is reflected in the good readability of the letters beneath it. The high WCA of the water droplets observed on the fabricated SPG₂ film is indicative of the superhydrophobicity of the film. Figure S6 in the Supporting Information shows the UV–vis transmittance spectra of micropatterned PG₂ and SPG₂ with different micropillar spacings. The transmittance of the PG₂ films increased with increasing pillar spacing, and changed slightly in the visible light range after siloxane functionalization. We also demonstrated that this type of film can be fabricated on glass instead of a PET film, with good conformality and high transparency (Figure S7, Supporting Information).

Flexibility of transparent superhydrophobic films with constant superhydrophobic properties is another important char-

acteristic for practical applications. The WCA of the fabricated SPG₂ film was tested as a function of different bending cycles (Figure 5c). One bending cycle constituted twisting the fabricated SPG₂ film (50 μm spacing) from its flat position to +180° to –180° with a bending radius ≈ 1.5 mm. As observed, the WCAs of the SPG₂ film were almost constant even after 1000 bending cycles without any significant changes (Video S1, Supporting Information). The optical transparency and superhydrophobicity of the SPG₂ film after repeated bending cycles were demonstrated by placing the film on a piece of paper with letters on it, and depositing water droplets as shown in the optical images in the inset of Figure 5c.

The mechanical durability of the fabricated SPG₂ was characterized through water-droplet impact and sand abrasion tests. The durability of the siloxane functionalization under long-term water-droplet impact was investigated by allowing water droplets to impinge the film from 10 cm at 45° (Figure S8a; Video S2, Supporting Information). The impact velocity of the water droplet was maintained at ≈ 1.44 m s^{–1}. Siloxane functionalization resulted in significant water resistance even after 14 050 μL of droplet impacts (Figure S8b, Supporting Information). After the water-droplet test, the SPG₂ film was allowed to dry naturally. The WCA of the SPG₂ film was found to be $\approx 150.6 \pm 1.3^\circ$ after impinging the surface with water droplets in volumes ranging from 14 000 to 14 080 μL (Figure 5d; Figure S8c, Supporting Information). The stable WCA of the SPG₂ film after the water-droplet impact reflects the excellent hydrophobicity of the film under water-droplet impact.

The long-term stability of the fabricated film was confirmed by measuring the WCA of the SPG₂ film aged in air for 14 days. The WCA was measured for 14 days in defined time intervals (Figure S9, Supporting Information). The fabricated material exhibited almost the same WCAs without any significant changes, indicating the long-term durability of the fabricated film. A sand abrasion test was carried out to examine the robustness of the fabricated SPG₂ film.

The film surface was impacted by ≈ 20 g of commercial sand (diameter: 50 to 900 μm) from a height of 25 cm (2.25 m s^{–1}) at 45° (Figure S10a, Supporting Information). After the sand impact test, the SPG₂ film surface was washed gently with water droplets. The WCA of the SPG₂ film following the sand abrasion test was found to be $\approx 145.3^\circ$ (Figure S10b, Supporting Information). The SPG₂ film retained its self-cleaning ability after sand abrasion, indicating that the siloxane-functionalized surface is suitable for practical outdoor applications (Video S3, Supporting Information).

The superior self-cleaning nature of the fabricated SPG₂ film was compared with that of the commercial PDMS elastomer. The sand abrasion test was conducted on the PDMS elastomer and SPG₂ film under the same experimental conditions as described in the previous sections. Subsequently, the films were washed gently with water and allowed to dry naturally. The WCAs of the PDMS elastomer and the SPG₂ film after the sand abrasion test were $\approx 110.78^\circ$ and 145.3° , respectively. The surfaces of both films were investigated by FE-SEM analysis to understand the reason for the excellent self-cleaning ability of the SPG₂ film (Figure S10, Supporting Information). After the sand impingement test, the structure of SPG₂ remained intact,

and few nanoscale sand particles had adhered on the surface (Figure S11a–c). In contrast, several nanoscale sand particles were found on the PDMS surface (Figure S11d–f, Supporting Information). This abundance of sand particles on the PDMS surface was primarily responsible for the loss of hydrophobicity of the PDMS film.

The self-cleaning properties of the fabricated SPG₂ film were verified by dripping water droplets onto the surface contaminated by sand (diameter: 50–550 μm) (Figure S12a; Video S4, Supporting Information). The glass slide-supported fabricated film was placed at 30° relative to the horizontal line (Figure S12b,c, Supporting Information). On contacting the sand powders, the water droplets rolled off and carried away the dust particles (Figure S12d, Supporting Information). The self-cleaning properties of the SPG₂ film were also tested by blowing a gentle wind (Figure S13; Video S5, Supporting Information). First, 0.5 g of sand (50–550 μm) was randomly shaken onto the SPG₂ film. Subsequently, the sand powder was blown away through a gentle wind by squeezing a 5 mL plastic dropper. Although the surface was covered by a large pile of sand (2 g), it became very clean after this action. We also conducted the same experiment with the PDMS elastomer (Figure S13; Video S5, Supporting Information). Results show that a large amount of sand powder adhered on the surface of PDMS even after the film was lifted with a tweezer to shake off the sand. These tests further indicate that a siloxane-functionalized surface has advantages over the PDMS elastomer in practical outdoor applications of superhydrophobic materials, particularly surfaces that are exposed to sand or dust.

2.4. Solar Cell Applications

The feasibility of using the fabricated HTFS and its advantages over the commercial PDMS elastomer were investigated using the J – V curves of the electronic devices with and without the protective film, as shown in Figure 6. The insets in Figure 6 show the corresponding photovoltaic performance for each case. The measurements were carried out under three conditions, as described in the Experimental Section. The PCEs of a bare solar module under different conditions were found to be $\approx 8.90\%$, 8.36% , and 8.80% , respectively. The PCEs of the PDMS elastomer and fabricated SPG₂-protected solar module under different conditions were $\approx 9.41\%$, 8.37% , 8.97% , and 9.10% , 8.99% , and 9.10% , respectively. The PCEs of the PDMS elastomer and SPG₂-protected solar modules were higher than that of the bare solar cell module. The performance improvement of the protected solar module is due to the high optical transparency and light-trapping effect of the periodically arranged micropillars on the surface of the protective film, which reduce light reflectance. Scheme S1 in the Supporting Information schematically illustrates the light-trapping effect of the fabricated film. When light irradiates the bare solar cell surface, most of it is directly absorbed by the solar cell; however, a small portion of the light is inevitably reflected (Scheme S1a, Supporting Information). Owing to the high transmittance of the fabricated SPG₂ film, most of the light is transmitted from air to the SPG₂ film and reaches the solar cell; however, a small portion of the light is reflected by the adjacent micropillars when light irradiates the SPG₂

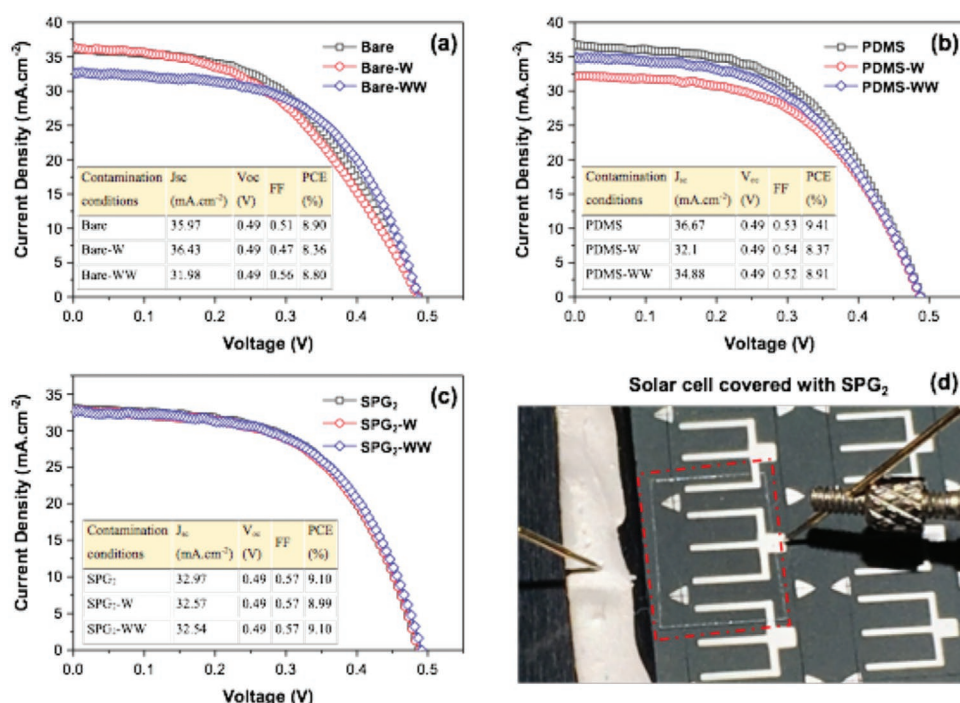


Figure 6. a) J – V curves of a) an unprotected (bare) solar module, b) solar module protected by an unmodified PDMS film, c) solar module protected by the fabricated SPG₂ film under different contamination conditions, and d) optical image of one part of the solar module protected by the SPG₂ film. Insets in (a)–(c) show the PCE of the solar module obtained from the corresponding J – V curves. W and WW denote the contaminated surface after wind cleaning, and wind cleaning combined with water-droplet cleaning, respectively.

film-protected solar cell at different angles (Scheme S1b, Supporting Information). Therefore, the SPG₂ film-protected solar cell would absorb more light compared to the bare solar cell, resulting in an increased PCE. The slightly higher PCE of the solar cell covered by the PDMS elastomer compared to that of the solar cell protected by the SPG₂ film is due to the higher transmittance of the former, as observed in UVDRS analysis. The PCEs of the solar modules protected by PDMS (PDMS-W) and SPG₂ (SPG₂-W) decreased to 8.37% and 8.99%, respectively. The significantly reduced PCE of the PDMS-covered cell compared to that of the SPG₂-covered cell demonstrates that the fabricated siloxane-functionalized film has better self-cleaning properties under a gentle wind than the PDMS elastomer. After washing with water, the PCEs of the bare, PDMS, and SPG₂ solar modules recovered to 8.80%, 8.91%, and 9.10%, respectively. As observed, the PCE of the SPG₂-protected solar module recovered to its initial value compared to that of the bare and PDMS-protected solar modules, due to the superior superhydrophobicity of the fabricated SPG₂ film. The hydrophobicity of the PDMS elastomer was not recovered. Hence, we believe that the fabricated SPG₂ film is an ideal protective layer for optical and electronic devices.

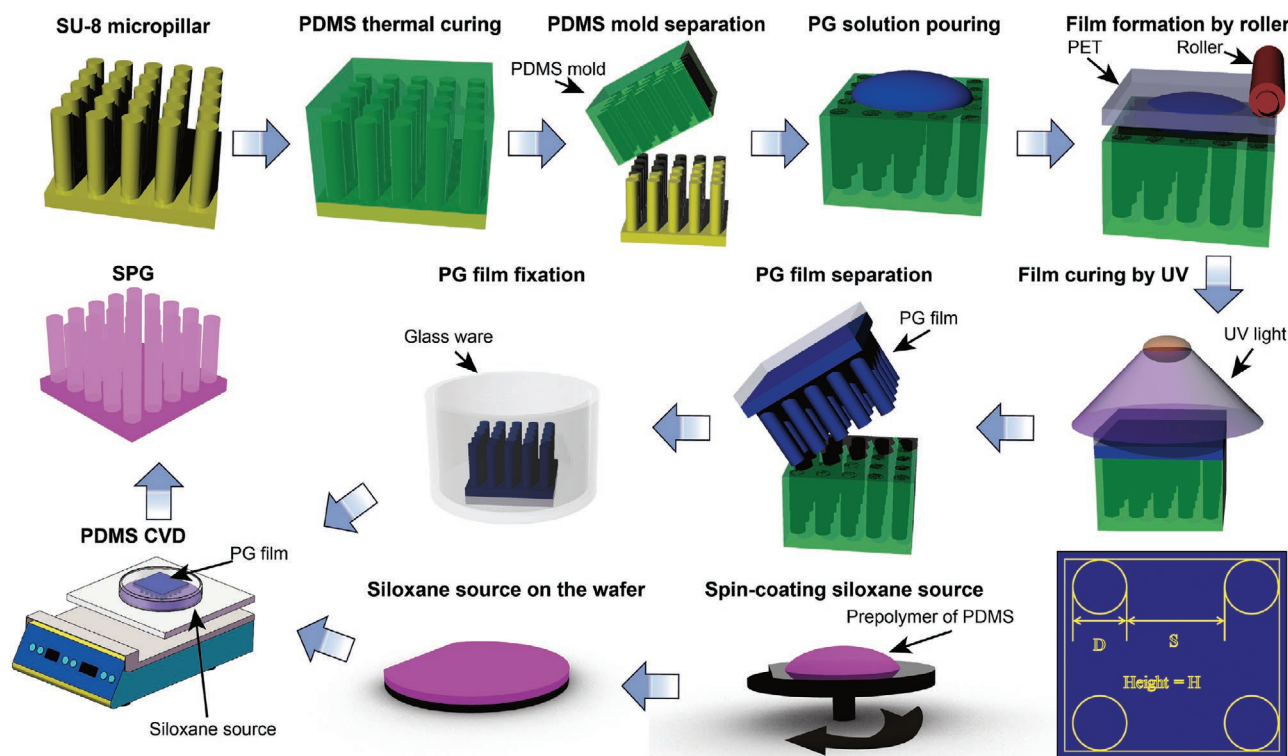
3. Conclusion

In summary, a highly flexible, transparent, self-cleaning, superhydrophobic, and durable film was fabricated by com-

binning micropatterning and siloxane functionalization through PDMS CVD. The micropatterned film was fabricated using a UV-curable PG composite. The inherent hydrophilic nature of PG changed to superhydrophobic through siloxane functionalization on the micropatterned PG surface. The superhydrophobicity of the prepared film was confirmed through WCA measurements, including WACA, WCA, WRCA, SA, water-droplet impact, and self-cleaning tests. The superhydrophobic nature of the fabricated film was retained without any degradation after repetitive bending cycles, indicating the robustness and high flexibility of the film. The film also showed optical transparency higher than ≈84% in the visible light region. Further, the fabricated film showed excellent self-cleaning ability and mechanical durability during the sand abrasion test. The practical applicability of the fabricated SPG₂ film was demonstrated by using the film as a protective layer for a solar module. The PCE of the solar cell covered by the SPG₂ film (9.10%) was higher than that of the bare solar cell (8.90%). The obtained data indicate that the HTFS film developed herein can be used as a protective layer for optical devices that require flexibility and high transparency.

4. Experimental Section

Fabrication: The SPG-based superhydrophobic film was fabricated through a mold transfer process followed by surface functionalization with siloxane (Scheme 2). The fabrication process is detailed below.



Scheme 2. Schematic illustration of the fabrication process flow of highly transparent, flexible, and self-clean superhydrophobic (HTFS) films. The inset in the bottom right corner denotes the top view of geometry of periodically placed micropillars (D , H , and S are the diameter, height, and spacing of the micropillars, respectively).

Preparation of Micropatterned PDMS Mold: First, the micropatterned SU-8 positive mold was fabricated using the modified photolithography technique described in the Supporting Information. The micropattern was then transferred to PDMS. The PDMS (Sylgard 184, Dow Corning, Midland, MI, USA) mixture was prepared by mixing its base and a curing agent in a ratio of 10:1. The mixture was then placed in a vacuum desiccator (F42025) for 30 min for degassing. Subsequently, it was poured on the micropatterned SU-8 positive mold and degassed in a desiccator for 30 min followed by curing at 80 °C for 4 h on a hotplate in an atmospheric condition. Finally, the PDMS negative mold was obtained by peeling off from the master mold.

Preparation of Micropatterned PG Film: The transparent and flexible micropatterned PG film was prepared by a facile replica molding process. In a typical fabrication process, a calculated amount of the as-prepared UV-curable PG composite was deposited onto the PDMS mold. A $\approx 100\ \mu\text{m}$ thick PET film was then attached to the PG liquid drop as a supportive handling layer. Subsequently, the PG liquid drops were deposited on the PDMS mold using a roller to force out the air bubbles inside the PG. The PDMS mold-deposited PG was then exposed to UV light with an energy of $\approx 180\ \text{mJ cm}^{-2}$. Finally, the cured PG film was carefully demolded from the PDMS mold. The contents of GO in the PG solution were 0.05, 0.1, and 0.2 wt%, and the corresponding films were named PG₁, PG₂, and PG₃, respectively. Finally, PG₂ (with 0.1 wt%) was used in subsequent experiments considering the transparency of the PG films and the abundance of functional groups provided by GO, as described in Figure S14 (Supporting Information).

Preparation of Siloxane-Functionalized Micropatterned PG Film: In a typical fabrication process, the PDMS prepolymer was spin-coated on a 4 in. clean Si wafer at 600 rpm for 30 s. The micropatterned PG film fabricated in the preceding section was attached to the glassware. The siloxane source of PDMS was coated on a Si wafer and placed on a hot plate, which was preheated to 296 °C (285 °C at the PDMS source and 175 °C at the sample surface). Subsequently, the PG supported by the glassware was placed above the preheated PDMS for siloxane functionalization. The optimized temperature and deposition time were 285 °C and 2 h, respectively, and the corresponding optimization processes are described in Figures S15–S17 and Table S2, Supporting Information). After the reaction, the deposition kit was naturally cooled. The siloxane-functionalized PG₁, PG₂, and PG₃ films were named SPG₁, SPG₂, and SPG₃, respectively.

All SPG samples were purified with ethanol solution in an ultrasonication bath for 30 min to remove the unreacted siloxane before characterization, unless otherwise specified in the present work.

Solar Cell Application: The feasibility of the fabricated HTFS film (SPG₂) as a protective layer for a CZTSSe-based custom-made solar cell module was verified. PDMS elastomer was used as a reference protective layer. The PCEs of the bare solar cell and solar cells protected by different films were characterized under different conditions using a Class AAA solar simulator (WXS-155S-L2, WACOM, and Japan) with AM 1.5G and 100 mW cm⁻², at 25 °C. The current–voltage (*J*–*V*) curves of the bare cell as well as the cells protected by the PDMS elastomer and SPG₂ film were characterized under three conditions: cleaning, sand contamination, and cleaning with a gentle wind (the sand powder that remained on the PDMS after the blowing the gentle wind was vigorously shaken off by hand before solar cell measurement), and sand contamination followed by cleaning with a gentle wind and water droplets.

Supporting Information

Supporting Information is available from the Wiley Online Library or from the author.

Acknowledgements

This work was supported by a National Research Foundation of Korea grant funded by Korea government (MSIP) (No. 2017R1E1A1A01074550),

and the Korea Health Technology R&D Project through the Korea Health Industry Development Institute (KHIDI) funded by the Ministry of Health & Welfare (No. HI19C0642).

Conflict of Interest

The authors declare no conflict of interest.

Keywords

graphene oxide, poly(urethane acrylate), siloxane functionalization, solar cell protection layers, superhydrophobic

Received: April 29, 2020

Revised: July 6, 2020

Published online:

- [1] A. M. A. Mohamed, A. M. Abdullah, N. A. Younan, *Arabian J. Chem.* **2015**, *8*, 749.
- [2] Y.-Y. Quan, L.-Z. Zhang, R.-H. Qi, R.-R. Cai, *Sci. Rep.* **2016**, *6*, 38239.
- [3] Y. Y. Yan, N. Gao, W. Barthlott, *Adv. Colloid Interface Sci.* **2011**, *169*, 80.
- [4] a) I. Banerjee, R. C. Pangule, R. S. Kane, *Adv. Mater.* **2011**, *23*, 690; b) C. Hellio, D. Yebra, *Advances in Marine Antifouling Coatings and Technologies*, Elsevier, Amsterdam **2009**.
- [5] a) S. S. Latthe, C. Terashima, K. Nakata, M. Sakai, A. Fujishima, *J. Mater. Chem. A* **2014**, *2*, 5548; b) Y. Lai, Y. Tang, J. Gong, D. Gong, L. Chi, C. Lin, Z. Chen, *J. Mater. Chem.* **2012**, *22*, 7420.
- [6] a) J. Huang, S. Wei, L. Zhang, Y. Yang, S. Yang, Z. Shen, *Materials* **2019**, *12*, 1155; b) M. Nosonovsky, B. Bhushan, *Multiscale Dissipative Mechanisms and Hierarchical Surfaces: Friction, Superhydrophobicity, and Biomimetics*, Springer Science & Business Media, Berlin/New York **2008**.
- [7] a) J. Gu, P. Xiao, J. Chen, F. Liu, Y. Huang, G. Li, J. Zhang, T. Chen, *J. Mater. Chem. A* **2014**, *2*, 15268; b) J. Meng, S. Lin, X. Xiong, *Prog. Org. Coat.* **2017**, *107*, 29.
- [8] a) F. Mumm, A. T. J. van Helvoort, P. Sikorski, *ACS Nano* **2009**, *3*, 2647; b) J. Zhou, S. Yang, X. Y. Zeng, J. H. Wu, G. P. Chen, Y. P. Huang, *J. Adhes. Sci. Technol.* **2012**, *26*, 2087.
- [9] a) I. S. Bayer, A. Steele, P. J. Martorana, E. Loth, *Appl. Surf. Sci.* **2010**, *257*, 823; b) J. I. Lim, S. I. Kim, Y. Jung, S. H. Kim, *Polymer* **2013**, *37*, 411.
- [10] a) Y.-B. Park, H. Im, M. Im, Y.-K. Choi, *J. Mater. Chem.* **2011**, *21*, 633; b) S. J. Choi, S. Y. Huh, *Macromol. Rapid Commun.* **2010**, *31*, 539.
- [11] B. Sahoo, K. Yoon, J. Seo, T. Lee, *Coatings* **2018**, *8*, 47.
- [12] a) M. Hikita, K. Tanaka, T. Nakamura, T. Kajiyama, A. Takahara, *Langmuir* **2005**, *21*, 7299; b) K. Tadanaga, K. Kitamuro, A. Matsuda, T. Minami, *J. Sol-Gel Sci. Technol.* **2003**, *26*, 705.
- [13] K. Teshima, H. Sugimura, Y. Inoue, O. Takai, A. Takano, *Appl. Surf. Sci.* **2005**, *244*, 619.
- [14] a) D. Kontziampasis, G. Boulousis, A. Smyrnakis, K. Ellinas, A. Tserepi, E. Gogolides, *Microelectron. Eng.* **2014**, *121*, 33; b) Z. Han, Z. Wang, B. Li, X. Feng, Z. Jiao, J. Zhang, J. Zhao, S. Niu, L. Ren, *ACS Appl. Mater. Interfaces* **2019**, *11*, 17019.
- [15] a) M. Im, H. Im, J.-H. Lee, J.-B. Yoon, Y.-K. Choi, *Soft Matter* **2010**, *6*, 1401; b) R. Dufour, M. Harnois, Y. Coffinier, V. Thomy, R. Boukherroub, V. Senez, *Langmuir* **2010**, *26*, 17242; c) D. Gong, J. Long, D. Jiang, P. Fan, H. Zhang, L. Li, M. Zhong, *ACS Appl. Mater. Interfaces* **2016**, *8*, 17511.
- [16] J. Park, B. Q. H. Nguyen, J.-K. Kim, A. Shanmugasundaram, D.-W. Lee, *Jpn. J. Appl. Phys.* **2018**, *57*, 06HJ09.

- [17] J. G. Kim, H. J. Choi, K. C. Park, R. E. Cohen, G. H. McKinley, G. Barbastathis, *Small* **2014**, *10*, 2487.
- [18] N. Vourdas, A. Tserepi, E. Gogolides, *Nanotechnology* **2007**, *18*, 125304.
- [19] H. Lei, J. Xiao, M. Xiong, Z. Liping, Z. Qixin, *Coatings* **2019**, *9*, 159.
- [20] R. C. Buck, J. Franklin, U. Berger, J. M. Conder, I. T. Cousins, P. Voogt, A. A. Jensen, K. Kannan, S. A. Mabury, S. P. J. Leeuwen, *Integr. Environ. Assess. Manage.* **2011**, *7*, 513.
- [21] B. Q. H. Nguyen, A. Shanmugasundaram, T.-F. Hou, J. Park, D.-W. Lee, *Chem. Eng. J.* **2019**, *373*, 68.
- [22] J. Coates, *Encyclopedia of Analytical Chemistry: Applications, Theory and Instrumentation*, Wiley, New York **2006**.
- [23] B. Jana, A. Biswas, S. Mohapatra, A. Saha, S. Ghosh, *Chem. Commun.* **2014**, *50*, 11595.
- [24] J. Wu, P. Wang, F. Wang, Y. Fang, *Nanomater* **2018**, *8*, 864.
- [25] W. S. O'Shaughnessy, M. Gao, K. K. Gleason, *Langmuir* **2006**, *22*, 7021.
- [26] K. Jiao, C. Zhou, N. Becerra-Mora, J. Fiske, P. Kohli, *J. Mater. Chem. C* **2016**, *4*, 8634.
- [27] J. González-Rivera, R. Iglío, G. Barillaro, C. Duce, M. R. Tinè, *Polymers* **2018**, *10*, 616.
- [28] J. Madejova, P. Komadel, *Clays Clay Miner.* **2001**, *49*, 410.
- [29] Y. Kebukawa, S. Nakashima, T. Otsuka, K. Nakamura-Messenger, M. E. Zolensky, *Meteorit. Planet. Sci.* **2009**, *44*, 545.
- [30] S. M. Hafiz, R. Ritikos, T. J. Whitcher, N. M. Razib, D. C. S. Bien, N. Chanlek, H. Nakajima, T. Saisopa, P. Songsiriththigul, N. M. Huang, *Sens. Actuators, B* **2014**, *193*, 692.
- [31] E. Rebollar, S. Pérez, M. Hernández, C. Domingo, M. Martín, T. A. Ezquerro, J. P. García-Ruiz, M. Castillejo, *Phys. Chem. Chem. Phys.* **2014**, *16*, 17551.
- [32] P. K. Kipkemboi, P. C. Kiprono, J. J. Sanga, *Bull. Chem. Soc. Ethiop.* **2003**, *17*, 211.
- [33] D. Cai, A. Neyer, R. Kuckuk, H. M. Heise, *J. Mol. Struct.* **2010**, *976*, 274.
- [34] R. Chen, T. Li, Q. Zhang, Z. Ding, P. Ma, S. Zhang, M. Chen, W. Dong, W. Ming, *New J. Chem.* **2017**, *41*, 9762.
- [35] K. C. Chang, C. H. Hsu, H. I. Lu, W. F. Ji, C. H. Chang, W. Y. Li, T. L. Chuang, J. M. Yeh, W. R. Liu, M. H. Tsai, *eXPRESS Polym. Lett.* **2014**, *8*, 243.
- [36] B. Yu, X. Wang, W. Xing, H. Yang, L. Song, Y. Hu, *Ind. Eng. Chem. Res.* **2012**, *51*, 14629.
- [37] D. H. Wang, Y. Hu, J. J. Zhao, L. L. Zeng, X. M. Tao, W. Chen, *J. Mater. Chem. A* **2014**, *2*, 17415.
- [38] A. Shanmugasundaram, V. Gundimeda, T. F. Hou, D. W. Lee, *ACS Appl. Mater. Interfaces* **2017**, *9*, 31728.
- [39] A. Shanmugasundaram, N. D. Chinh, Y. J. Jeong, T. F. Hou, D. S. Kim, D. Kim, Y. B. Kim, D. W. Lee, *J. Mater. Chem. A* **2019**, *7*, 9263.
- [40] a) Y. Y. Wang, K. Kusumoto, C. J. Li, *Phys. Procedia* **2012**, *32*, 95;
b) M.-P. Delplancke, J. M. Powers, G. J. Vandentop, M. Salmeron, G. A. Somorjai, *J. Vac. Sci. Technol., A* **1991**, *9*, 450.
- [41] B. Yu, X. Wang, X. Qian, W. Xing, H. Yang, L. Ma, Y. Lin, S. Jiang, L. Song, Y. Hu, *RSC Adv.* **2014**, *4*, 31782.
- [42] G. Beamson, D. Briggs, *J. Chem. Educ.* **1993**, *20*, 267.
- [43] S. Reiche, R. Blume, X. C. Zhao, D. Su, E. Kunkes, M. Behrens, R. Schlögl, *Carbon* **2014**, *77*, 175.
- [44] E. Njungab, R. Oum Lissouck, H. Ntede Nga, C. Labrugère, R. Pommier, L.-M. Ayina Ohandja, J. Noah Mgamveng, presented at *21ème Congrès Français de Mécanique, August 2013, Bordeaux, France (FR)* **2013**.
- [45] J. W. Krumpfer, T. J. McCarthy, *Langmuir* **2011**, *27*, 11514.
- [46] S. Wu, *Polymer Interface and Adhesion*, M. Dekker, New York **1982**.
- [47] G. Camino, S. M. Lomakin, M. Lazzari, *Polymer* **2001**, *42*, 2395.
- [48] B. Bhushan, Y. C. Jung, *Ultramicroscopy* **2007**, *107*, 1033.
- [49] N. A. Patankar, *Langmuir* **2003**, *19*, 1249.